Jiang, W. et al. (2022) Dielectric constant engineering of organic semiconductors: effect of planarity and conjugation length. *Advanced Functional Materials*, 32(3), 2104259.

The material cannot be used for any other purpose without further permission of the publisher and is for private use only.

There may be differences between this version and the published version. You are advised to consult the publisher's version if you wish to cite from it.

This is the peer reviewed version of the following article:

Jiang, W. et al. (2022) Dielectric constant engineering of organic semiconductors: effect of planarity and conjugation length. *Advanced Functional Materials*, 32(3), 2104259, which has been published in final form at: 10.1002/adfm.202104259

This article may be used for non-commercial purposes in accordance with Wiley Terms and Conditions for Self-Archiving.

https://eprints.gla.ac.uk/288632/

Deposited on 19 January 2023

Enlighten – Research publications by members of the University of Glasgow
http://eprints.gla.ac.uk

Dielectric Constant Engineering of Organic Semiconductors: Effect of Planarity and Conjugation Length

Wei Jiang,[1] Hui Jin,[1] Mohammad Babazadeh,[1] Alex S. Loch,[1] Aaron Raynor,[1] Neil Mallo,[1] David M. Huang,[2] Xuechen Jiao,[3] Wen Liang Tan,[3] Christopher R. McNeill,[3] Paul L. Burn,[1*] Paul E. Shaw[1]

[1] *Centre for Organic Photonics & Electronics (COPE), School of Chemistry and Molecular Biosciences, The University of Queensland, Brisbane, QLD 4072, Australia*

[2] *Department of Chemistry, School of Physical Sciences, The University of Adelaide, Adelaide South Australia, 5005, Australia*

[3] *Department of Materials Science and Engineering, Monash University, Clayton, Victoria 3800, Australia*

***Correspondence to:** p.burn2@uq.edu.au

Keywords:

Solar cells, organic semiconductors, homojunction, dielectric constant, molecular geometry.

Abstract

Bulk heterojunction organic solar cells continue to show steady photoconversion efficiency improvements. However, single component organic solar cells are a particularly attractive alternative due to the relative simplicity of device manufacture. It has been proposed that organic semiconductors with a high dielectric constant (≈10) could give rise to spontaneous free charge carrier generation upon photoexcitation. In this manuscript we have explored factors that affect the dielectric constant of organic semiconductors, particularly the optical-frequency dielectric constant. We compare the properties of monomers, dimers and trimers of two isoelectronic families of materials that have acceptor units composed of one or two dicyanovinylbenzothiadiazole moieties and one to three donor units. The donor components are composed of either fluorenyl or dithienocyclopentadiene moieties with the same glycol-based solubilising groups. We find that chromophore planarity and orientation with respect to the substrate, and film density affect the optical and electronic properties of the materials, especially the high-frequency dielectric constant. The results also indicate that delocalisation of the highest occupied and lowest unoccupied molecular orbitals is a critical factor. The dimer with two dicyanovinylbenzothiadiazole moieties and two dithienocyclopentadiene units was found to have the highest optical frequency dielectric constant and overall performance.

Introduction

The bulk heterojunction (BHJ) photoactive layers used in the most efficient organic solar cells are generally composed of at least one electron-donating material and one electron accepting material. The BHJ approach is used to overcome the exciton binding energy and maximise the efficiency of free-charge carrier generation.

In the past decade, the power conversion efficiency (*PCE*) of solution processed single active layer BHJ solar cells has steadily improved, reaching up to 18%.[1] The improvement in BHJ solar cell performance has arisen through a combination of materials design, particularly the development of non-fullerene acceptors,[2-4] as well as improvements in device architecture engineering[5] and post-processing methods.[2] Key to the BHJ solar cell efficiency is control of the active-layer film morphology,[6-7] with a delicate balance between the donor and acceptor interfacial area (required for exciton separation) and connected pathways for the free charges to be extracted from the device. However, the performance of a BHJ is sensitive to variations in morphology, which leads to issues with regard to reproducibility in terms of efficiency and device lifetime,[8] as well as providing challenges for device scaling, that is, when moving from laboratory testing to large-scale manufacturing. Therefore, in spite of the tremendous efficiencies reported for BHJ solar cells there would be a distinct longer-term advantage of designing materials that could be used in single-component organic solar cells (SCOSCs),[9,10] that is, solar cells that have a single material in the light-absorbing layer.[11]

The two current approaches to SCOSCs include materials composed of linked donor and acceptor chromophores (an intramolecular "bulk heterojunction") and materials that have been designed to have a high dielectric constant. Of these two approaches the former is the most advanced in terms of examples of materials and device performance.[12-15] The structures of the linked donor and acceptor materials have predominantly had either oligomeric donors connected to fullerene acceptors[9-10] or donor polymer cables with perylene diamine acceptor chromophores.[14,15] The latter approach has led to a strategy of morphology control through thermally driven self-organised phase separation, with good device stability under long-term illumination being demonstrated.[15]

An alternative less developed approach is based on an understanding of the Wannier-Mott model, which describes the exciton binding energy as inversely proportional to the dielectric constant ($E_b \propto 1/\varepsilon^2$). It has been postulated that if the organic semiconductor materials could be designed with an high dielectric constant ($\varepsilon \approx 10$) that organic semiconductors could have Wannier-Mott like excitons.[16] If that could be achieved then free charge carriers would be generated upon photoexcitation[17] in a similar manner to inorganic[19] and hybrid semiconductor materials.[20,21] However, the dielectric constant of a material is frequency dependent and a key question to consider in the development of such materials is which frequency or frequencies are critical for charge generation and/or extraction. An early and commonly reported strategy to increase the dielectric constant has been to replace the alkyl groups normally used to solubilise organic semiconductors with ethylene glycol moieties.[22-23] This approach was particularly successful in increasing the ε at low-frequency (ε_{lf}) due to enhanced dipole polarisability, with an ε_{lf} as high as 9.8 being reported for a small molecule.[22] An important outcome of the early work on increasing the low-frequency dielectric constant was that the ethylene glycol moieties did not change the fundamental spectral, electronic or charge-transporting properties of the materials.[22,24,25] Subsequent work reported that the optical frequency dielectric

constant (ε_{opt}) was important for the direct generation of free charge carriers upon photoexcitation.[26,27] There a number of factors that can affect the optical frequency dielectric constant, including chromophore conjugation length and orientation (with respect to the substrate), the dipole moment of the material, and film density.[28] There has been one report showing the effect of conjugation length, whereby the optical frequency dielectric constant of a dimeric material composed of two dithienocyclopentadiene "donor" and two dicyanovinylbenzothiadiazole "acceptor" units was found to be higher than the corresponding monomer material (one of each). The optical frequency dielectric constant was found to increase from 3.6 to 4.6, and interestingly, homojunction solar cells showed that charges were generated more efficiently near the optical gap for the dimer.[26] That is, the results imply that extending the conjugation length can lead to an increased optical frequency dielectric constant and more efficient charge generation. However, the *PCEs* of these homojunction devices have yet to be reported. A further outcome of the early study was that solar cells composed of the glycolated equivalents of the monomer and dimer materials had higher external quantum efficiencies near the absorption onset compared to their alkylated equivalents. One potential explanation for this latter result is that the flexibility of the glycol side chains leads to less steric hindrance,[25,29] resulting in closer π-π stacking and thus a higher film density.[26]

In this manuscript we comprehensively explore the effect of the chromophore conjugation length and planarity on the optoelectronic properties of two families of isoelectronic semiconductor materials. The materials have acceptor units composed of one or two dicyanovinylbenzothiadiazole moieties and one to three donor units. The donor components are composed of either fluorenyl or dithienocyclopentadiene moieties with the same glycol-based solubilising groups **Figure 1**. We report the dielectric constants of the materials and how these relate to their chemical and electronic structure, and film morphology. Finally, we show how the planarity, and chromophore conjugated length and type affects the charge transport properties of the materials and their performance in homojunction solar cells.

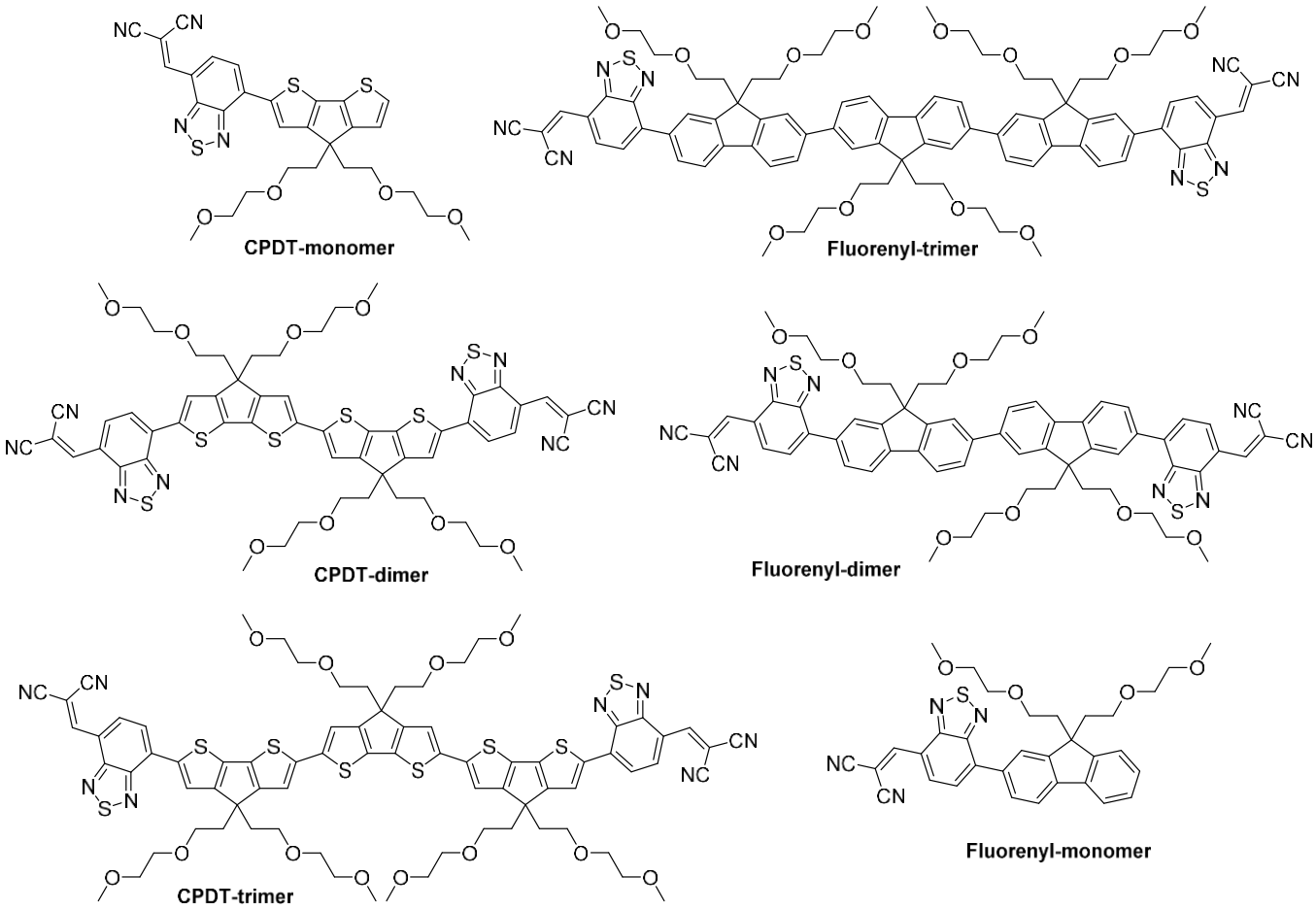

Figure 1. Structures of the compounds compared in this study.

Results and discussion

Synthesis

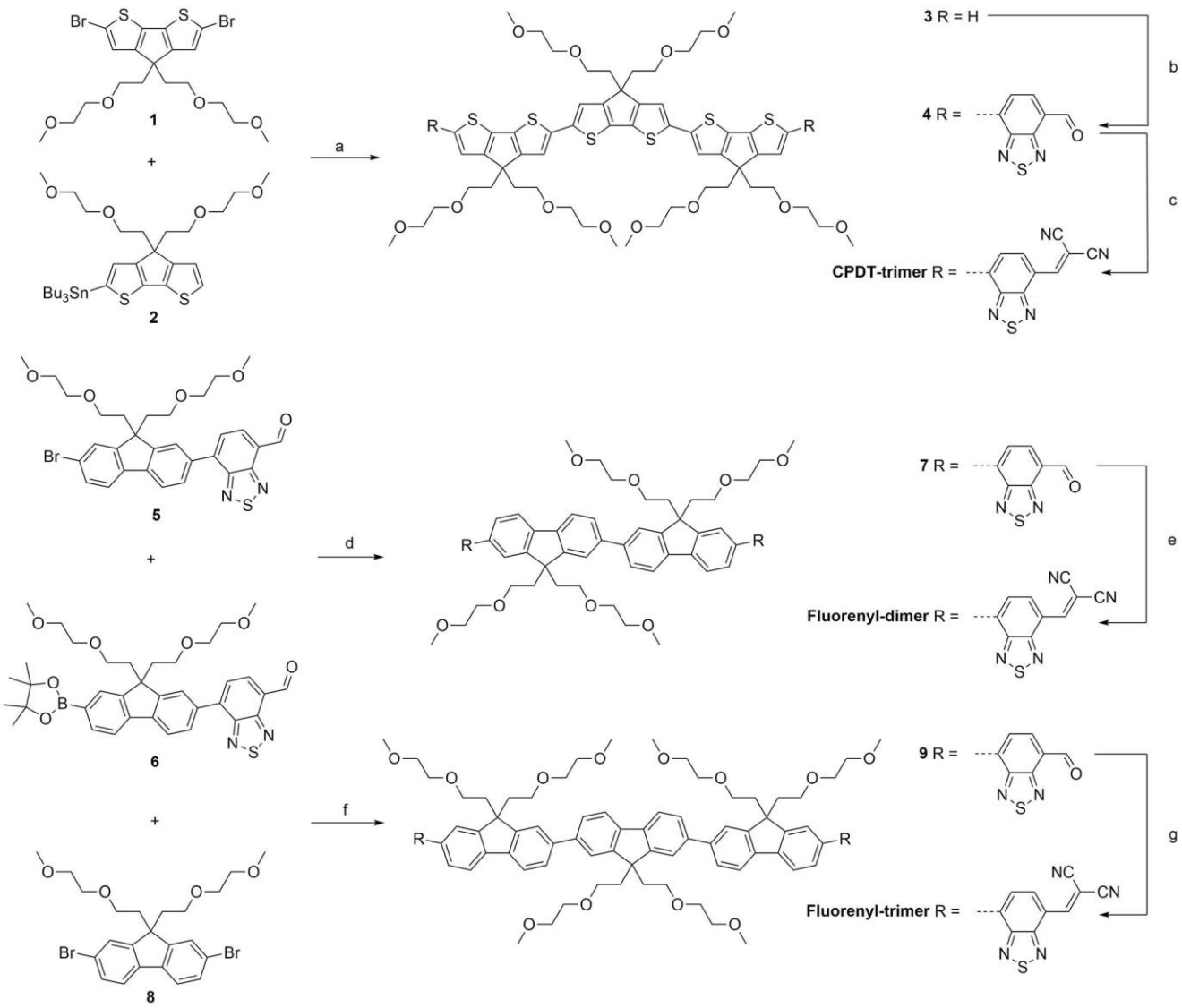

Scheme 1. Synthesis of **CPDT-trimer**, and **Fluorenyl-dimer** and **-trimer**. Reagents, conditions and yields: a) $Pd(PPh_3)_2Cl_2$, toluene, reflux, 21 h, 20%; b) 1) *n*-butyllithium, tetrahydrofuran, -78 °C, 1 h, then, tri-*n*-butyltin chloride, room temperature, 1.5 h, then $Pd(PPh_3)_4$, toluene, reflux, 16 h, 40%; c) malononitrile, pyridine, toluene, 60 °C, 5 h, 56%; d) $Pd(PPh_3)_4$, K_2CO_3 (2M aq.), toluene, *t*-BuOH, reflux, overnight, 59%; e) malononitrile, pyridine, chlorobenzene, 75 °C, overnight, 37%; f) $Pd(PPh_3)_4$, Cs_2CO_3, toluene, reflux, 22 h, 35%; g) malononitrile, pyridine, chloroform, reflux, 3.5 h, 62%.

The syntheses of the **CPDT-monomer**[22] and **CPDT-dimer**[26] and **Fluorenyl-monomer**[22] have been previously reported. The synthetic pathways to the **CPDT-trimer** and **Fluorenyl-dimer** and **-trimer** from reported intermediates are shown in **Scheme 1**. The first step in the synthesis of the **CPDT-trimer** was the Stille coupling of **1**[26] and **2**[22] to form trimer **3**, which was achieved a 20% yield. Trimer **3** was converted to the bis-stannyl derivative and then reacted under palladium-catalysed Stille conditions with 7-bromobenzo[*c*][1,2,5]thiadiazole-4-carbaldehyde to give **4** in a 40% yield. The final step required the condensation of **4** with malononitrile, with the **CPDT-trimer** being formed in an isolated yield of 56%. The syntheses of the **Fluorenyl-dimer** and **-trimer** utilised a similar strategy, with **5** being the key intermediate. **5** was formed in an 52% yield through a chemoselective Suzuki reaction between 2-bromo-7-iodo-9,9-bis[2-

(2-methoxyethoxy)ethyl]-*9H*-fluorene (see Supporting Information) and 7-(4,4,5,5-tetramethyl-1,3,2-dioxaborolan-2-yl)benzo[*c*][1,2,5]thiadiazole-4-carbaldehyde.[30] To prepare the **Fluorenyl-dimer** and **-trimer**, **5** was converted into the corresponding boronate ester **6**, which due its instability was then used immediately. In the case of the **Fluorenyl-dimer**, **5** was reacted with **6** to form dialdehyde **7** (59% yield) and then in the final step **7** underwent a Knoevenagel condensation with malononitrile, giving the **Fluorenyl-dimer** in a 37% yield. For the synthesis of the **Fluorenyl-trimer**, **6** was reacted with the glycolated dibromofluorene derivative **8** to give dialdehyde **9** in a 35% yield. Finally, 9 was condensed with malononitrile to give the Fluorenyl-trimer in a 62% yield. Gel permeation chromatography showed that the compounds were monodisperse and increased in size from monomer to trimer across both series and that there were no low molecular weight components in the dimers and trimers (**Figures S1** and **S2**).

Film density and morphology

To set the framework for the differences in the optoelectronic properties of the materials we first determined how the materials packed in films using X-ray reflectometry (XRR) and grazing-incidence wide angle X-ray scattering (GIWAXS) measurements to determine the density and π-stacking distances. The density of the CPDT-based monomer, dimer and trimer from XRR measurements were 1.23 g/cm^3, 1.29 g/cm^3 and 1.29 g/cm^3, respectively. Apart from the **Fluorenyl-monomer** (1.23 g/cm^3), the density of the **Fluorenyl-dimer** and **Fluorenyl-trimer** (1.13 g/cm^3) were lower than their CPDT counterparts. The scattering patterns from the GIWAXS measurements of the dimers and trimers of both families are shown in **Figure 2**. The **CPDT-dimer** and **-trimer** exhibit reflections that are indexed to lamellar stacking (100) and π-π stacking (010) peaks at ~0.42 Å^{-1} and 1.8 Å^{-1}, respectively. The appearance of the (100) peaks in-plane and (010) peaks out-of-plane indicate that the CPDT-based materials adopt a face-on orientation with respect to the substrate. The appearance of the (100) peak at ~0.42 Å^{-1} corresponds to a lamellar (side-chain) stacking repeat distance of ~ 15 Å, while the appearance of the (010) peak at 1.77 Å^{-1} corresponds to a π–π stacking distance of 3.55 Å for both CPDT-based molecules. The (100) and (010) peaks for the **CPDT-dimer** are both narrower than those of the **CPDT-trimer** indicating that the dimer (see **Figure S3** in the Supporting Information) has improved crystallinity (either larger crystallites and/or reduced crystalline disorder). In contrast, the fluorenyl-based materials are essentially amorphous, indicated by the lack of well-defined scattering features. A very broad ring centred at ~1.6 Å^{-1} is seen, characteristic of weakly correlated π-π stacking corresponding to an average π–π stacking distance of 4.0 Å, which is consistent with the lower film density. The fluorenyl-based materials also exhibit a lack of texture indicating a lack of preferential molecular orientation in thin film. Based on the structural analysis and the criteria postulated to affect the optical-frequency dielectric constant [chromophore conjugation length and orientation (with respect to the substrate), and film density][28] it might be expected that the CPDT-based materials would outperform the fluorenyl-containing compounds across a range of the critical optoelectronic metrics.

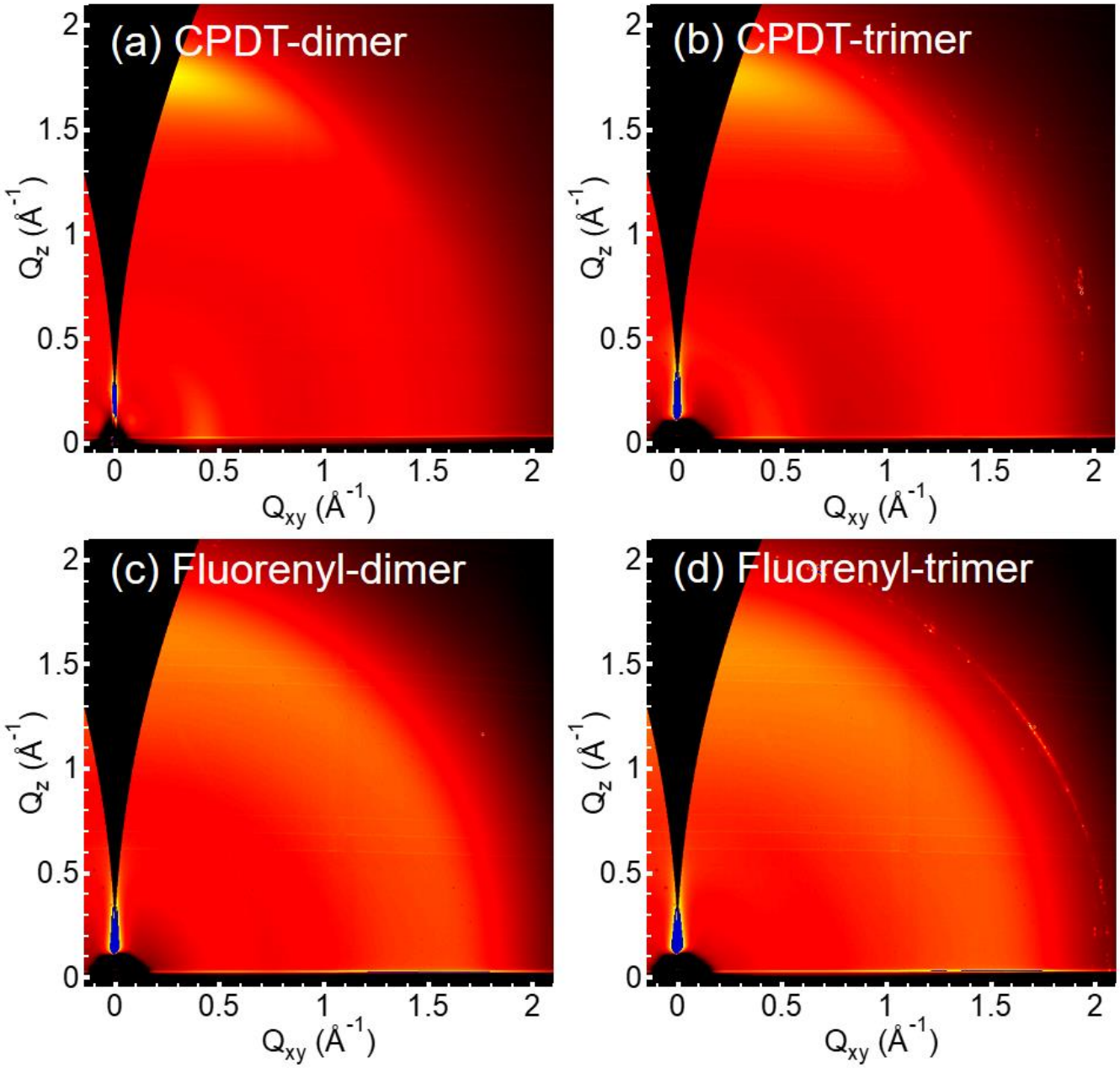

Figure 2. 2D GIWAXS patterns of neat films of **CPDT-dimer** (a) and **-trimer** (b) and **Fluorenyl-dimer** (c) and **-trimer** (d) cast from chloroform solutions onto silicon substrates.

Molecular orbital calculations

To gain insight into the differences in densities and π-stacking distances between the different materials classes, we undertook density functional theory (DFT) calculations. The starting structure in each case had the molecule in a planar arrangement, which was then allowed to relax to its lowest energy ground-state geometry using the B3LYP functional and DZP Slater-type basis set in the gas phase, with the results for the dimers and trimers shown in **Figure 3**. For computational efficiency the glycol units were replaced by methyl groups. The key difference between the CPDT- and fluorenyl-based materials was that the former had greater planarity overall. That is, the dihedral angle between the benzothiadiazole and CPDT unit was 0.04° (compared to 38° for the fluorenyl-benzothiadiazole unit) and the dihedral angle between the CPDT units

was only 18° compared to 44° for the **Fluorenyl-dimer**. The results are logical in that the steric interactions of the protons that lead to the twisting between the adjacent units would be expected to be less for the CPDT moieties than the fluorenyl units. The fact that the **CPDT-dimer** and **-trimer** are more planar than their fluorenyl counterparts is also consistent with the measured higher film density and smaller π-stacking distance for the former. A further consequence of the difference in the planarity of the two families of materials is the distribution of the highest occupied (HOMO) and lowest unoccupied molecular orbitals (LUMO) in the ground-state structures shown in **Figure 3**. For the **CPDT-dimer** there is HOMO and LUMO density on both the CPDT and benzothiadiazole moieties. In contrast, the **Fluorenyl-dimer** has the HOMO and LUMO density strongly localised on the fluorenyl and benzothiadiazole units, respectively. For the **CPDT-trimer** the HOMO is delocalised over all five units while the LUMO has no density on the central CPDT-unit. In the case of the **Fluorenyl-trimer**, the HOMO had greatest density on the central fluorenyl moiety and little delocalisation of the LUMO across any of the fluorenyl units. Finally, the HOMO–LUMO gap was found to decrease for both families in moving from the dimer to the trimer.

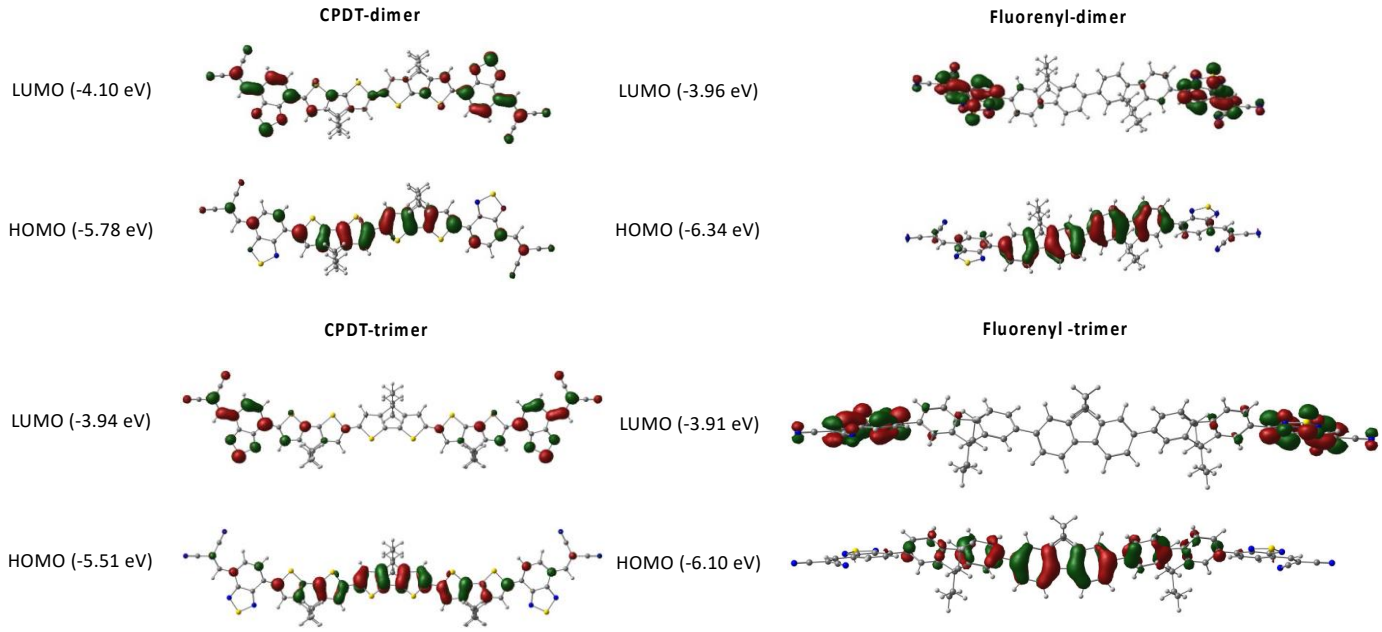

Figure 3. Molecular orbitals of the CPDT- and fluorenyl-based dimers and trimers showing the HOMO and LUMO distributions.

We also undertook time-dependent DFT (TD-DFT) calculations of the lowest energy singlet absorption transition in the monomer, dimer, and trimer of both the CPDT and fluorenyl series starting from the optimised gas-phase ground-state geometry. The calculations were carried out with the Tamm–Dancoff (TDA) approximation at the B3LYP/TZP level in both the gas phase and in a dielectric medium using the conductor-like screening model (COSMO). All calculations were performed using the Amsterdam Density Functional (ADF) package (ADF 2019.301).[31] To match the properties of the dichloromethane (DCM) solvent in which solute-phase absorption spectra were measured, the static and optical dielectric constants in the dielectric medium calculations were set respectively to $\varepsilon = 8.9$, the default for DCM in ADF, and ε_{opt}

= n^2 = 2.0, where n is the refractive index of DCM.[32] The relationship between the optical properties and these calculations will be discussed in the next section.

Optical properties

In the next part of the analysis of the properties of the materials we compared the effect of extending the conjugation length of the two families on the absorption spectra (**Figure 4**). The solution absorption spectra of the CPDT series are shown in **Figure 4a** and it can be seen that in moving from the monomer to the dimer there is a significant red shift in the onset and peak of the long-wavelength absorption (λ_{max} from 595 nm to 724 nm), with a negligible change in moving to the trimer (λ_{max} = 726 nm). The fact that the long wavelength λ_{max} was not red shifted further for the trimer and its smaller molar extinction coefficient than the dimer is consistent with the molecular orbital calculations that showed there was no LUMO density on the central CPDT unit. A similar trend was observed for the fluorenyl series – there was a significant red shift in the long-wavelength absorption peak in moving from the monomer to the dimer (λ_{max} = 451 nm to 482 nm), whereas the λ_{max} for the trimer was at a similar wavelength to the dimer (λ_{max} = 479 nm) (**Figure 4b**). The onset of the absorption of the CPDT-based materials being at longer wavelengths than those of the fluorenyl-containing materials is consistent with the relative energy levels of the individual donor units (CPDT *versus* fluorene), the HOMO and LUMO energies from the DFT calculations, and TD-DFT calculations of the lowest energy absorption transition (**Table S1**). Consistent with the experiments, the TD-DFT calculations (both in the gas phase and dielectric medium) show a significant decrease in transition energy (increase in transition wavelength) from the monomer to dimer, but little change from the dimer to trimer. This behaviour can be rationalised based on the natural transition orbitals (NTOs) for this transition (**Figures S4** and **S5**), which show that, upon photoexcitation, charge transfer occurs from CPDT/fluorene units to the dicyanovinylbenzothiadiazole unit in both the dimers and trimers, with the initial ("hole") orbital and final ("electron") orbital involved in the transition delocalised to a similar extent in the dimers and trimers. The calculations are also qualitatively consistent with the decrease in oscillator strength from dimer to trimer in both the CPDT and fluorenyl series.

a) b)

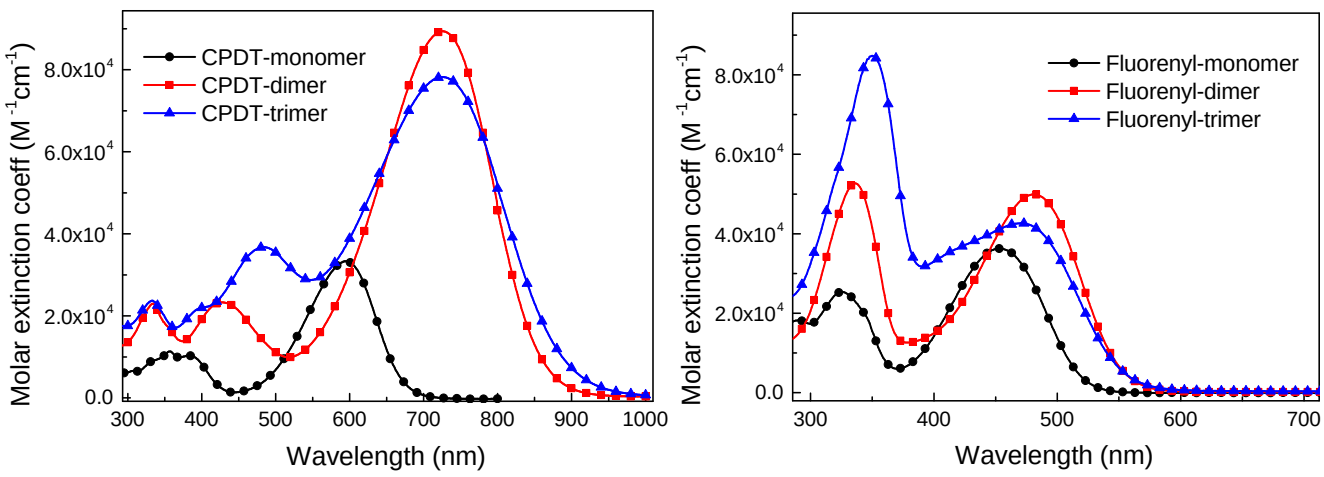

c) d)

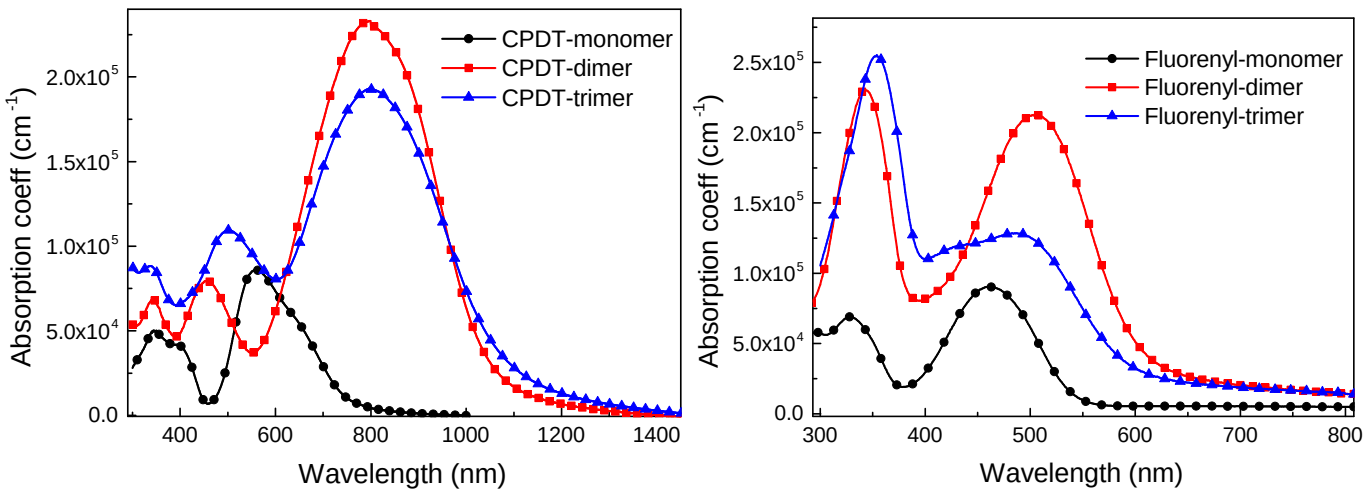

Figure 4. Molar extinction coefficient as a function of wavelength for solutions of the CPDT (a) and fluorenyl (b) series, and absorption coefficient as a function of wavelength for films of the CPDT (c) and fluorenyl (d) series.

The behaviour of the absorption spectra of the two families were completely different when moving to the solid state. In the case of the fluorenyl series there was a small red shift in the onset of the absorption and long-wavelength peak, which is normally ascribed to slight planarisation of the chromophores in the film (**Figure 4d**). In contrast, for the CPDT family of materials there was a red shift in the absorption onset, which was significant (>100 nm) for the dimer and trimer, with the film absorption in both cases going beyond 1100 nm (1.1 eV) (**Figure 4c**). In the case of the **CPDT-monomer**, while the onset to the absorption was red shifted the peak maximum was blue shifted compared to solution, which could arise from H-aggregation in the solid state. Planarisation of the chromophore alone would not be expected to give rise to such a large red shift and hence the observed changes in the absorption spectra of the CPDT-based dimer and trimer are likely to be due to a combination of planarisation and their propensity to π-stack, as observed from the X-ray scattering experiments.

Electronic properties

The redox properties of the materials were determined in solution using cyclic voltammetry (see **Figure S6**), with the $E_{1/2}$s reported against the ferrocene/ferrocenium couple and the results summarised in **Table 1**. The CPDT-based materials were found to undergo chemically reversible oxidations (one, two and three, respectively) and two chemically reversible reductions. In contrast, only the **Fluorenyl-monomer** underwent a chemically reversible oxidation, with the monomer, dimer and trimer undergoing one, two and two chemically reversible reductions, respectively. The first oxidation (for the monomer) and reduction potentials of the fluorenyl-based materials were at more positive and negative potentials compared to those of the CPDT containing materials, which is consistent with the trend in the calculated HOMO and LUMO energies. The thin film ionisation potentials (IPs) of the materials were also measured using photoelectron

spectroscopy in air (PESA) (**Table 1**). The IPs of the fluorenyl-based materials we found to be larger (5.7-5.9 eV) than those of the compounds composed of the CPDT units (5.0-5.3 eV).

Table 1 Summary of the optical and electronic properties of the materials.

Materials	CPDT-			Fluorenyl-		
	monomer	**dimer**	**trimer**	**monomer**	**dimer**	**trimer**
λ_{max} (solution/film, nm)	595/559	724/793	726/802	451/464	481/507	471/490
IP (eV)	5.3	5.0	5.0	5.9	5.9	5.7
$E_{1/2(ox)}$ (V)	0.5	0.2, 0.9	0.05, 0.2, 0.9	0.6	–	–
$E_{1/2(red)}$ (V)	-1.2	-1.1, -1.5	-1.1, -1.7	-1.3	-1.2, -1.8	-1.2, -1.8, -2.1
Optical gap (eV)	1.9	1.2	1.1	2.4	2.2	1.9

The dielectric constants of the materials were then determined using charge extraction with linearly increasing voltage (CELIV) and impedance measurements for ε_{lf}, and a combination of spectroscopic reflectometry, transmission and ellipsometry for ε_{opt}, with the results shown in **Table 2** and pictorially in **Figure S7**. The optical-frequency dielectric constant was higher for all the CPDT materials compared to the equivalent fluorenyl-based materials for films of similar thickness (around 50 nm), with the **CPDT-dimer** and **-trimer** having the highest ε_{opt} of 4.6. However, it should be noted that the optical-frequency dielectric constant was dependent on film thickness up to around 50 nm (as shown in **Table S2**), after which it remained unchanged. As a consequence, we used films that had thicknesses of around 40-50 nm for the photovoltaic devices. At this point it is worth remembering the characteristics that are proposed to be critical for a molecule to have a high optical frequency dielectric constant, namely, chromophore conjugation length (π-delocalisation) and orientation (with respect to the substrate), and film density.[28] Based on these criteria it is not surprising that the fluorenyl family of materials have the smaller optical frequency dielectric constants. The X-ray scattering data show that the **Fluorenyl-dimer** and **-trimer** have the lower density and larger π–π stacking distance when compared to their CPDT counterparts. Furthermore, the GIWAX data show that the films composed of the **Fluorenyl-dimer** and **-trimer** are amorphous with no preferential orientation of the chromophore with respect to the substrate. In contrast, the **CPDT-dimer** and **-trimer** have a preferred face-on orientation with respect to the substrate. Perhaps the more surprising result is that the optical frequency dielectric constant of the **CPDT-trimer** is not larger than the dimer despite of its larger conjugated framework. In the case of the **CPDT-dimer** the HOMO and LUMO density is distributed across all the sub-units. However, while the HOMO of the **CPDT-trimer** is delocalised over the trimer chromophore, the

LUMO is not, with the central ring bereft of LUMO density. These results suggest that to increase the dielectric constant both the HOMO and LUMO need to be as fully delocalised as possible.

Finally, before fabricating homojunction solar cells we measured the hole and electron mobilities of the dimers and trimers using metal-insulator-semiconductor charge extraction by linear increasing voltage (MIS-CELIV), with the results shown in **Table 2** and **Figure S8**. The two monomers were previously reported to have similar electron mobilities (≈10^{-6} cm^2/Vs) but did not have a measurable hole mobility.[22] In fact, using MIS-CELIV we did not observe any hole mobility for the fluorenyl-based materials. Interestingly, for the fluorenyl-series, increasing the conjugation length of the chromophore led to a decrease in the electron mobility. Presumably this arises from the fact that the LUMO density is strongly localised on the end dicyanovinylbenzothiadiazole units of the molecules leading to decreased probability of intermolecular overlap of these units as they become a smaller component of the overall molecule (i.e., there are larger numbers of fluorenyl units). In contrast, both the **CPDT-dimer** and **-trimer** have measurable hole mobilities of order ≈10^{-5} cm^2/Vs, with the dimer having an order of magnitude higher electron mobility at 1 ×10^{-4} cm^2/Vs. The electron mobility of the **CPDT-trimer** is over an order of magnitude lower than the dimer at 6.5 × 10^{-6} cm^2/Vs, which would be consistent with the more localised nature of the LUMO of the former, decreasing the probability of intermolecular LUMO overlap in the thin film.

Table 2 Summary of the electronic properties, diode mobility, film density, π-stacking distance and homojunction device parameters of the compounds for comparison in this study.

Materials	**CPDT-**			**Fluorenyl-**		
	monomer	**dimer**	**trimer**	**monomer**	**dimer**	**trimer**
ε_{lf}	9.8	6.1	5.1	8.5	3.5	5.0
ε_{opt}	3.6	4.6	4.6	2.9	3.0	3.0
μ_h (cm^2/Vs)	–	1.25 × 10^{-5}	1.5 × 10^{-5}	–	–	–
μ_e (cm^2/Vs)	3.0 × 10^{-6}	1.0 × 10^{-4}	6.5 × 10^{-6}	1.3 × 10^{-6}	1.4 × 10^{-8}	4.2 × 10^{-7}
Density (g/cm^3)	1.23	1.29	1.29	1.23	1.15	1.13
π-stacking distance (Å)	3.88	3.59	3.58	3.92	3.83	4.05
EQE (%) at the absorption peak	0.5	4.2	1.6	0.8	1.2	1.3
J_{sc} (mA/cm^2)	0.06±0.00	1.11±0.03	0.57±0.02	0.02±0.00	0.15±0.01	0.17±0.01
V_{oc} (V)	0.32±0.06	0.56±0.02	0.31±0.03	0.29±0.06	0.58±0.04	0.71±0.10
FF (%)	30.4±1.4	34.9±0.6	33.6±0.4	32.4±2.3	25.0±0.7	23.2±1.2

PCE (%)	0.006±0.002	0.21±0.01	0.06±0.01	2×10^{-3}±0.00	0.02±0.00	0.03±0.00
Hero *PCE* (%)	0.008	0.23	0.06	0.002	0.025	0.03

Devices

Based on the optical and electronic properties it would be expected that CPDT-based materials would provide better performance in homojunction solar cells. The CPDT-materials absorb across a broader wavelength range, have higher optical frequency dielectric constants, and in the case of the **CPDT-dimer** and **-trimer** are capable of both hole and electron transport. Homojunction devices with structure ITO/PEDOT:PSS/homojunction/Ca/Al were fabricated and tested, with the EQEs *versus* absorption spectra shown in **Figure 5a-5f**, current density versus voltage (*J*–*V*) in **Figure S9**, and a summary of the device characteristics in **Table 2**. A key feature of all the devices was that independent of the ε_{opt} they all generated charge near the optical gap, with those of the **CPDT-dimer** and **-trimer** having the highest EQE near the optical gap. The devices comprising the monomers showed diode characteristics but low performance, which can at least in part be ascribed to the lack of hole mobility and poor electron mobility. **The CPDT-dimer** showed good diode characteristics and low dark current leakage. In contrast, the **Fluorenyl-dimer** (and indeed **-trimer**) had very poor performance, but they also had the lowest electron mobilities and no measurable hole mobility. The performance of the devices containing the **CPDT-trimer** compared to the **CPDT-dimer** were limited by the fact that the former had a smaller absorption coefficient (note the films in both devices were of similar thickness) and its electron mobility was almost two orders of magnitude smaller than that of the dimer. It has been previously reported that the slower charge mobility can affect charge generation and hence efficiency.[33] Nevertheless, these results suggest that there might be a minimal ε_{opt} to achieve charge generation near the optical gap, with the higher the ε_{opt} the more efficient the process. The homojunction device containing the **CPDT-dimer** was found to have the highest photoconversion efficiency (*PCE*) of 0.23%. While this is low compared to the state-of-the-art intramolecular BHJ SCOSCs, it is comparable to the very early reports of non-fullerene acceptor-based devices.[34-36] The **CPDT-dimer** devices had the largest J_{sc} (consistent with the relative high film absorption coefficient and onset >1100 nm) and *FF* (consistent with the higher and more balanced electron and hole mobilities). A clear trend was that the more disordered and poorly aligned a material was (relative to the substrate) the poorer the device performance.

(a) (d)

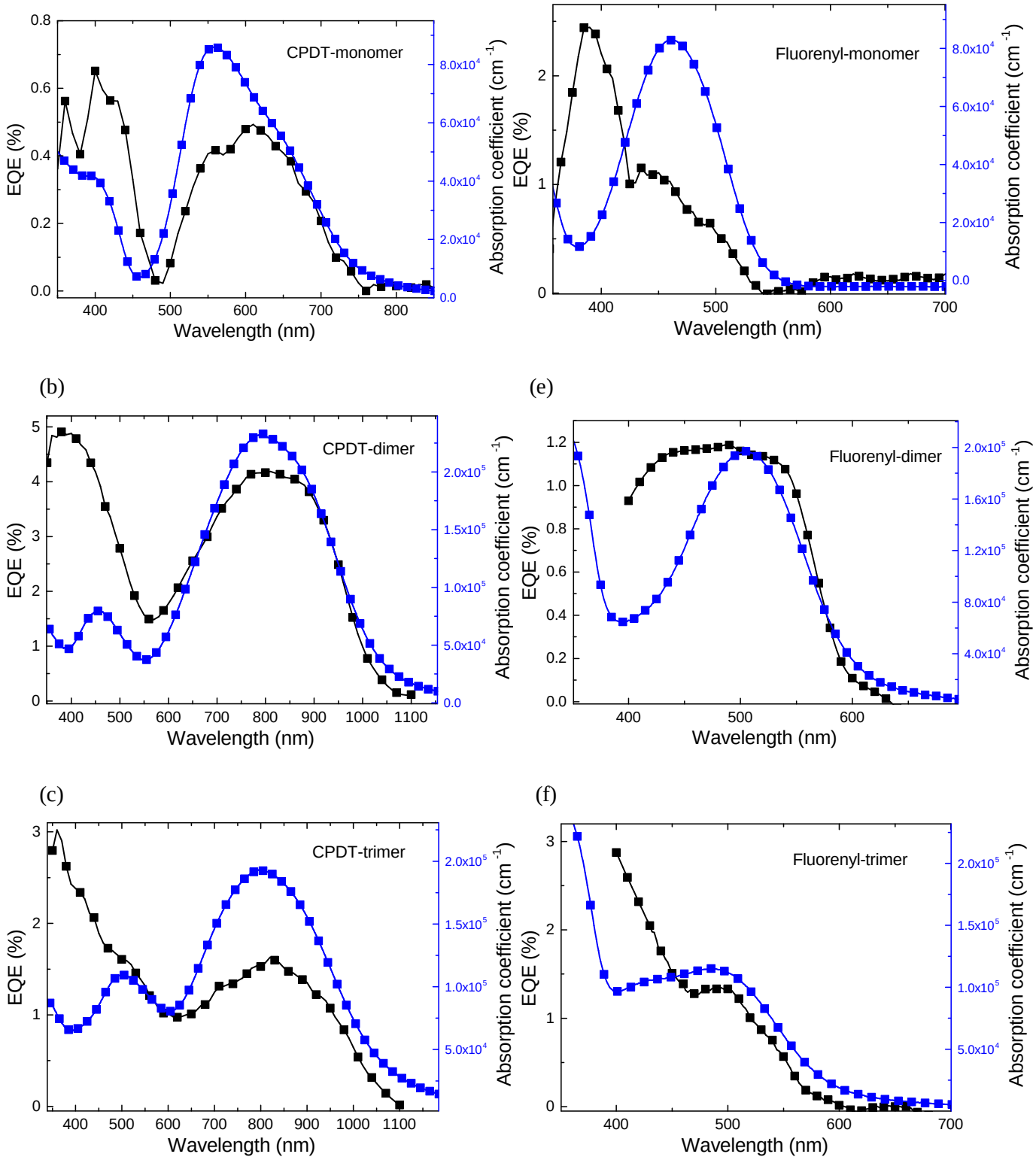

Figure 5. Film absorption spectra and external quantum efficiency (EQE) of homojunction devices with a structure of ITO/PEDOT:PSS/homojunction/Ca/Al composed of **CPDT-monomer** (a), **-dimer** (b) and **-trimer** (c), and **Fluorenyl-monomer** (d), **-dimer** (e) or **-trimer** (f).

In order to gain greater insight into the photovoltaic performance we employed steady-state intensity dependent photocurrent (IPC) measurements at short-circuit conditions for the better performing CPDT-based devices. The slower carrier mobility is a key parameter for device performance as it determines the maximum extractable photocurrent prior to significant photocarrier recombination losses that scale with the

second-order of the light intensity - in other words, the space charge limited photocurrent (I_{SCLC}).[37] It has been shown that the IPC allows quantification of the non-geminate recombination losses with such a non-linear recombination order (i.e., "bimolecular" recombination losses).[37,38] **Figure S10** shows the normalized EQE (setting the generation and absorption efficiency to 100%) versus the photocurrent under short circuit conditions, which enables quantification of the charge transport/collection efficiency losses due to bimolecular recombination. It can be seen from **Figure S10** that the homojunction devices containing **CPDT-dimer** and **-trimer** only showed small losses due to bimolecular recombination when excited at 532 nm. This implies that the low photoconversion efficiencies is likely to arise from overall poor charge generation.

Conclusions

We have developed two families of materials designed to provide a framework and insight into the creation of high optical frequency dielectric constant materials that could be used in simple homojunction organic solar cells. While a number of factors that can affect the optical frequency dielectric constant have been proposed, including chromophore conjugation length and orientation (with respect to the substrate), and film density, there has not been a sufficient body of evidence as to which of these are most important. Our results show that the planarity of the chromophore is critical to achieving the desired properties. Planarity increases molecular orbital delocalisation, the film density and the possibility of favourable orientation of the chromophore with respect to the substrate, leading to increased light absorption, film crystallinity, and charge mobility. However, the results show that increasing the conjugation length does not always lead to an increase in dielectric constant or an improvement in the optoelectronic properties, which appears to be directly related to the degree of molecular orbital delocalisation. The dimer with two dicyanovinylbenzothiadiazole moieties and two dithienocyclopentadiene was found to have the highest optical-frequency dielectric constant, relatively balanced and reasonable hole and electron mobilities and best overall homojunction device performance. While the photoconversion efficiency of the device was significantly lower than current state-of-the-art organic solar cells it is interesting note that early non-fullerene-acceptor-based devices had similar performance. In conclusion, the results from this work add extra key criteria that need to be considered when developing high dielectric constant materials for homojunction organic solar cells.

Experimental

Material Synthesis and Characterisation. Commercial materials were used as received unless otherwise stated. Dichloromethane used for the optical measurements was dried over calcium hydride or potassium carbonate and distilled immediately prior to use. Dichloromethane (HPLC grade, ≥99.9%) and methanol (HPLC grade, ≥99.9%) used for the mass spectroscopy measurements were used as received from Sigma Aldrich®. Dichloromethane for column chromatography was distilled by rotary evaporation under reduced pressure before use. Column chromatography was performed with Merck silica, 230-400 mesh. When solvent

mixtures are used, the proportions are given by volume. Medium pressure liquid chromatography (MPLC) was performed on a Grace Reveleris X2 system using silica or C18 reverse-phase cartridges. Size-exclusion column chromatography was performed with Bio-Rad Bio-Beads S-X1, 200-400 mesh.

^{1}H and ^{13}C NMR spectra were recorded on Bruker AS500, AV500 or AN300 spectrometers. Chemical shifts are reported in parts per million (ppm) and are referenced to the residual solvent peak ($CDCl_3$ 7.26 ppm for ^{1}H or 77.0 ppm for ^{13}C, and CD_2Cl_2 5.32 ppm for ^{1}H or 53.8 ppm for ^{13}C). Gl−H = H on glycol solubilising groups, CPDT−H = dithienocyclopentadienyl H, Fl−H = fluorenyl H, BT−H = benzothiodiazolyl H, and VIN−H = vinyl H. Multiplicities are reported as singlet (s), doublet (d), doublet of doublets (dd), and multiplet (m) and coupling constants (*J*) are given to the nearest 0.5 Hertz (Hz). High resolution electrospray ionisation (HRMS) accurate mass measurements were recorded in positive mode on a Bruker MicroTOF-Q (quadrupole time-of-flight) instrument with a Bruker ESI source. Elemental analyses were carried out using a Carlo Erba NCHS Analyser Model NA 1500 instrument at the School of Chemistry and Molecular Biosciences, The University of Queensland. Infrared (IR) absorption spectra were measured on a Perkin-Elmer Spectrum 100 FT-IR spectrometer as neat samples using an ATR crystal. Differential Scanning Calorimetry (DSC) was performed on PerkinElmer® Pyris Diamond DSC. Thermogravimetric analysis (TGA) was carried out on a Perkin-Elmer STA 6000 Simultaneous Thermal Analyser. Decomposition temperatures (T_d) are reported for a 5% decrease in mass. Melting points were measured using a Büchi Melting Point B-545 and are uncorrected. Absorption spectra were measured using a Varian Cary 5000 UV-vis-NIR spectrophotometer in double distilled dichloromethane (calcium hydride or potassium carbonate) at molar concentrations ranging between 10^{-5}–10^{-6} M or spun onto quartz substrates (from chloroform or chlorobenzene) at 5 mg/mL (≈10^{-3} M) for all the solid-state measurements, all of which were below the maximum solubility of the materials (≈10^{-2} M). Absorbance shoulders are denoted as sh. Cyclic voltammetry measurements were carried out on a BASi Epsilon Analyzer at room temperature in an electrolyte solution of 0.1 M tetra-*n*-butylammonium perchlorate in argon-purged anhydrous tetrahydrofuran or dichloromethane. Glassy carbon working, platinum auxiliary, and silver/silver nitrate in acetonitrile reference electrodes were used, and the $E_{1/2}$ values are quoted relative to the ferrocene/ferrocenium couple. Electrodes were polished between measurements with a polishing pad wetted with deionised water. The ionisation potentials were measured using Photoelectron Spectroscopy in Air (PESA) on a Riken Keiki AC-2 PESA spectrometer with a power setting of 5-10 nW and a power number of 0.5.

Device Characterisation. 20 Ohm square^{-1} indium tin oxide (ITO) coated glass substrates (Xinyan, Hong Kong) were pre-cleaned using an Alconox (detergent) solution held at 70 °C before being sonicated in sequence with Alconox, de-ionised water, acetone and 2-propanol for 6 min each. The substrates had dimensions of 2.5 cm × 2.5 cm with six 0.2 cm^2 active area pixels. A 30 nm PEDOT:PSS layer was spin-coated onto the cleaned ITO glass followed by baking at 150 °C for 15 mins in the air, and then the active material solutions were spin-coated onto the PEDOT:PSS layer in an MBraun glove box with oxygen concentration < 1 ppm and water concentration < 1 ppm. Solutions of the active materials were prepared in

chloroform at a concentration of 10 mg/mL. The solutions were filtered and then diluted to 5 mg/mL with chloroform. The solutions were spin-coated at 1000 rpm for 30 s to give films with a thickness of around 40-50 nm. The films were not thermally annealed after spin-coating and the thicknesses were measured using a Veeco Dektak 150 profilometer. Finally, 15 nm Ca and 100 nm Al were sequentially thermally deposited under a 10^{-6} mbar vacuum.

The devices were tested into a nitrogen filled MBraun glove box with oxygen and water concentrations of <1 ppm. Current-voltage (*J-V*) characteristics were acquired using a Keithley 2400 Source Measurement Unit with a 4-wire configuration to eliminate the effect of the cable resistances and SMU internal impedance in the measurement circuit. The simulated Air Mass 1.5 Global (AM 1.5 G) illumination was provided by an Abet ABA Sun 2000 Solar Simulator. The illumination intensity of 1.3 sun used for the organic solar cell measurements was set using a paired Newport calibrated meter in conjunction with an unfiltered silicon reference cell. Due to higher IR intensity, the 1.3 sun illumination from an unfiltered silicon reference cell was required such that 1 sun illumination corresponding to KG5 Si reference cell could be obtained and the J_{SC} from the organic solar cells equalled that determined from the integrated EQE. The *J-V* curves were measured on at least six devices to provide relevant statistics. An aperture of 0.2 cm^2 was applied during illumination test. The external quantum efficiency (EQE) spectra were recorded with a PV Measurement QEX7 setup, which was calibrated using an NREL certified photodiode and operated without white light bias and chopped and locked in the small perturbation limit.

Mobility measurements. The diode mobility for the neat films and blend films were measured using MIS-CELIV. An arbitrary waveform generator (Agilent 33250A) was used to generate the CELIV triangle pulse with adjustable voltage slope, offset and pulse length. The signal was recorded using a digital storage oscilloscope (LeCroy Waverunner A6200). The MIS-CELIV devices were fabricated with a structure of ITO/BCB (30 nm)/MgF_2 (40 nm)/semiconductor layer/Al for electron mobility and ITO/BCB (30 nm)/MgF_2 (40 nm)/semiconductor layer/MoOx/Ag for hole mobility. The thickness of the semiconductor layer for the MIS-CELIV measurements was around 150 nm.

Dielectric constant measurements. An Agilent E4980A LCR meter at an amplitude of 10 mV was used to measure the capacitance of devices with an area of 0.2 cm^2 and the thickness of ~1 μm to determine the "static" or low frequency dielectric constants at frequencies of between 20 Hz and 10^6 Hz. A device structure of ITO/semiconductor/Ag was used for the capacitance for the measurement. The shunt resistances of all of the samples tested were larger than 1 MΩ at low frequencies indicating negligible leakage. The real part of the refractive index (n) was determined from Kramers–Kronig transformations of the extinction coefficient (k) and base-lined with n (λ > 1200 nm) extracted from the spectroscopic ellipsometry data collected on a J. A. Woollam VUV-VASE ellipsometer. Dielectric constants in the high frequency regime (~10^{14} Hz) were converted from the optical constants (n and k). Finally, the real part of the dielectric constant spectrum as a function of optical frequency was calculated using n and k using the equation $\varepsilon_r = n^2 - k^2$.

Intensity Dependent Photocurrent (IPC) Measurements. Steady state IPC measurements were performed using a 532 nm continuous wave laser (Ningbo Lasever Inc.) providing a power of 1 W. Optical filters (ThorLabs) were used to attenuate the laser power and the photocurrent transients were recorded using an Agilent semiconductor device analyser (B1500A). Each measured data point corresponded to a steady state photocurrent measurement of the OSC at the respective incident laser power, which was simultaneously measured with a Silicon photodetector to improve the accuracy of the measurement.

GIWAXS measurements. GIWAXS measurements were conducted at the SAXS/WAXS beamline of the Australian Synchrotron.[40] Highly collimated 9 keV X-rays were calibrated to be at a tilt angle of 0 ± 0.01 degrees when parallel to the surface of each sample by use of a Silicon crystal analyzer. A Dectris Pilatus 1M detector collected 2D scattering patterns. Each scattering pattern was tiled together from three 1 second images with the detector slightly moved between exposures, such that the resulting image removes gaps between the detector modules. The sample to detector distance was measured using a silver behenate scattering standard. The scattering data reported were acquired at the critical angle identified as the angle with the highest scattering intensity. Data was analysed using a modified version of the NIKA small angle scattering analysis package.[41]

Synthesis.

4,4,4',4',4'',4''-Hexakis[2-(2-methoxyethoxy)ethyl]-4*H*,4'*H*,4''*H*-2,2':6',2''-tercyclopenta[2,1-*b*:3,4-*b*']dithiophene (3)

A mixture of **1**[26] (354 mg, 0.66 mmol), **2** (940 mg, freshly prepared following the procedure described in [15], not purified) and bis(triphenylphosphine)palladium(II) dichloride (38 mg, 0.05 mmol) in anhydrous toluene (8 mL) was subject to a freeze-pump-thaw cycle followed by backfilling with argon. The mixture was heated at reflux under argon in the dark for 21 h. When the reaction mixture had cooled to room temperature, diethyl ether (20 mL) was added and then mixture was washed with brine (50 mL). The isolated aqueous fraction was extracted with dichloromethane (3 × 30 mL). The combined organic fractions were dried over anhydrous sodium sulfate and filtered through a plug of Celite®. The filtrate was collected, and the solvent removed. The crude product was purified in several steps: first, using size exclusive column chromatography over Biobeads™ with tetrahydrofuran as eluent; second, size exclusion column chromatography over Biobeads™ with toluene as eluent; third, using MPLC containing a C18 reverse-phase cartridge with methanol:acetonitrile mixtures as eluent (3:1 to 0:1); and finally, recrystallisation by dissolving the compound in diethyl ether followed by cooling the solution in a dry ice/2-propanol bath to afford **3** as a dark red colour powder (127 mg, 20%); m.p.: 75–76 °C; λ_{max} (CH_2Cl_2/nm): 266 (log ε/dm^3 mol^{-1} cm^{-1} 4.00), 311sh (3.75), 324 (3.85), 483 (4.60), 511sh (4.51); δ_H (500 MHz, $CDCl_3$): 2.29-2.34 (12H, m, Gl−CH_2), 3.02-3.14 (12H, m, Gl−CH_2), 3.30-3.41 (42H, m, Gl−CH_2 and −CH_3), 6.97 (2H, d, J = 5.0 Hz, CPDT−H), 7.05 (2H, s, CPDT−H), 7.06 (2H, s, CPDT−H), 7.18 (2H, d, J = 5.0 Hz, CPDT−H); δ_C (125 MHz, $CDCl_3$): 37.5(8), 37.6(4), 49.6, 50.0, 59.0, 67.5(3), 67.5(5), 70.0, 70.1, 71.8, 117.3, 117.5, 121.7, 125.5, 134.9,

135.2, 136.4, 138.2, 138.7, 156.2, 156.8, 157.1; *m/z* (ESI-HRMS) anal. calcd. for $C_{57}H_{74}O_{12}S_6$ $[M]^+$: 1142.3499 (100%), 1143.3533 (62%), 1144.3457 (27%), 1145.3491 (17%), 1146.3524 (5%); found: 1142.3510 (56%), 1143.3564 (100%), 1144.3564 (70%), 1145.3557 (43%), 1146.3561 (19%).

7,7'-[4,4,4',4',4'',4''-Hexakis(2-{2-methoxyethoxy}ethyl)-4*H*,4'*H*,4''*H*-(2,2':6',2''-tercyclopenta[2,1-*b*:3,4-*b*']dithiophene) -6,6''-diyl]bis[benzo[*c*][1,2,5]thiadiazole-4-carbaldehyde] (4)

A solution of **3** (100 mg, 0.09 mmol) in anhydrous tetrahydrofuran (10 mL) under argon was cooled in a dry ice/2-propanol bath. *n*-Butyllithium (2.5 M in hexanes, 0.1 mL) was added dropwise and then the reaction was stirred for 1 h with cooling in a dry ice/2-propanol bath. Tri-*n*-butyltin chloride (0.1 mL, 0.36 mmol) was added in one portion. The reaction solution was allowed to warm to room temperature and stirred for another 1.5 h. Deionised water (10 mL) was added to quench the reaction and the organic layer separated. The aqueous layer was extracted with diethyl ether (2 × 10 mL). The combined organic fractions were dried over anhydrous sodium sulfate, filtered, and the solvent was removed. The crude product was purified using size exclusion chromatography over BioBeads™ with tetrahydrofuran as eluent to afford the bis(tri-*n*-butylstannanyl) derivative as a dark red solid (70 mg), which was used immediately in the next reaction. A solution of the bis(tributylstannanyl) derivative (70 mg), 7-bromobenzo[*c*][1,2,5]thiadiazole-4-carbaldehyde (40 mg, 0.16 mmol) in anhydrous toluene (5 mL) was subject to a freeze-pump-thaw cycle followed by backfilling with argon. Tetrakis(triphenylphosphine)palladium(0) (5 mg, 0.004 mmol) was added, and the solution was heated at reflux under argon in an oil bath in the dark for 38 h. When the reaction mixture had cooled to room temperature, diethyl ether (20 mL) was added. The mixture was washed with brine (2 × 30 mL) and then the combined aqueous fractions were extracted with diethyl ether (30 mL). The combined organic fractions were dried over anhydrous sodium sulfate, filtered, and the solvent was removed. The crude product was purified by size exclusion column chromatography over Biobeads™ using a toluene:dichloromethane mixture (4:1) as eluent followed by reprecipitation from a mixture of dichloromethane:diethyl ether to afford **4** as a dark blue powder (51 mg, 40%); m.p.: 159–161 °C; λ_{max} (CH_2Cl_2/nm): 321 (log ε/dm^3 mol^{-1} cm^{-1} 4.14), 478 (4.32), 635 (4.72); IR (solid) ν/cm^{-1} = 1681 (C=O); δ_H (500 MHz, $CDCl_3$): 2.34-2.47 (12H, m, Gl−CH_2), 3.14-3.20 (12H, m, Gl−CH_2), 3.28 (12H, s, Gl−CH_3), 3.32 (6H, s, Gl−CH_3), 3.35-3.42 (24H, m, Gl−CH_2), 7.14 (4H, brs, CPDT−H), 7.98 (2H, brd, *J* = 8.0 Hz, BT−H), 8.22 (2H, d, *J* = 8.0 Hz, BT−H), 8.27 (2H, s, CPDT−H), 10.69 (2H, s, CHO); δ_C (125 MHz, $CDCl_3$): 37.6, 50.2, 50.3, 58.9(9). 59.0(3), 67.5(2), 67.5(6), 70.1, 71.7(9), 71.8(2), 117.5, 118.1, 122.2, 124.6, 124.7, 133.0, 133.8, 134.8, 135.6, 138.6, 139.0, 141.0, 142.2, 152.0, 153.9, 157.4, 157.5, 159.4, 188.4; *m/z* (ESI-HRMS) anal. calcd. for $C_{71}H_{78}N_4O_{14}S_8$ $[M]^+$: 1466.3275 (100%), 1467.3308 (77%), 1468.3233 (36%), 1469.3266 (28%); found: 1466.3285 (100%), 1467.3312 (86%), 1468.3296 (75%), 1469.3300 (43%), 1470.3286 (22%).

2,2'-[({4,4,4',4',4'',4''-Hexakis[2-(2-methoxyethoxy)ethyl]-4*H*,4'*H*,4''*H*-[2,2':6',2''-tercyclopenta[2,1-*b*:3,4-*b*']dithiophene]-6,6''-diyl}bis{benzo[*c*][1,2,5]thiadiazole-7,4-diyl}bis(methaneylylidene)]dimalononitrile (CPDT-trimer)

A mixture of **4** (40 mg, 0.03 mmol) and malononitrile (16 mg, 0.24 mmol) in anhydrous toluene (2 mL) was deoxygenated by placing under vacuum three times followed by backfilling with argon. Anhydrous pyridine (3 drops) was added to the reaction mixture before it was stirred in an oil bath held at 60 °C under argon for 5 h. When the reaction mixture was cooled to room temperature, dichloromethane (30 mL) was added, and the mixture was washed with brine (50 mL). The aqueous fraction was collected and extracted with dichloromethane (3 × 10 mL). The combined organic fractions were dried over anhydrous sodium sulfate, filtered, and the solvent was removed. The crude product was purified by size exclusive column chromatography over Biobeads™ using a toluene:dichloromethane mixture (3:1) as eluent followed by reprecipitation from a dichloromethane:diethyl ether mixture by cooling in a dry ice/acetone bath. The precipitate was collected at the filter, washed with cold diethyl ether (10 mL), and then dried under vacuum to afford **CPDT-trimer** as a black powder (24 mg, 56%); m.p.: 190–191 °C; λ_{max} (CH_2Cl_2/nm): 259 (log ε/dm^3 mol^{-1} cm^{-1} 4.47), 332 (4.37), 399 sh (4.34), 485 (4.56), 725 (4.89); λ_{max} (film/nm): 341, 504, 799; IR (solid) ν/cm^{-1} = 2221 (C≡N); δ_H (500 MHz, $CDCl_3$): 2.34-2.47 (12H, m, Gl−CH_2), 3.14-3.21 (12H, m, Gl−CH_2), 3.28 (12H, s, Gl−CH_3), 3.32 (6H, s, Gl−CH_3), 3.34-3.43 (24H, m, Gl−CH_2), 7.14 (2H, brs, CPDT−H), 7.16 (2H, s, CPDT−H), 7.97 (2H, brd, J = 8.0 Hz, BT−H), 8.32 (2H, s, CPDT−H), 8.76 (2H, d, J = 8.0 Hz, BT−H), 8.77 (2H, s, VIN−H); δ_C (125 MHz, $CDCl_3$): 37.6, 50.2, 50.4, 59.0(1). 59.0(4), 67.5(2), 67.5(5), 70.2, 71.8(0), 71.8(3), 80.5, 113.6, 114.3, 117.6, 118.3, 120.5, 122.5, 125.6, 130.8, 134.1, 134.7, 135.9, 138.6, 139.2, 141.9, 143.8, 150.8, 151.9, 154.6, 157.6, 158.1, 160.3; *m/z* (ESI-HRMS) anal. calcd. for $C_{77}H_{78}N_8O_{12}S_8$ $[M]^+$: 1562.3499 (100%), 1563.3533 (83%), 1564.3457 (36%), 1565.3491 (30%), 1566.3524 (12%); found: 1562.3532 (100%), 1563.3558 (92%), 1564.3548 (79%), 1565.3550 (46%), 1566.3540 (21%); $T_{d(5\%)}$: 316 °C; DSC (heating and cooling rate: 100 °C min^{-1}): T_m = 195 °C (1st cycle − heating), 175 °C (2nd and 3rd cycles – heating), not present in the 4th cycle heating; $T_g \approx 93$ °C (2nd and subsequent cycles – heating); CV: $E_{1/2(ox)}$ (dichloromethane): 0.05 V, 0.2 V, 0.9 V; $E_{1/2(red)}$ (tetrahydrofuran): -1.1 V, -1.7 V.

7-[7-Bromo-9,9-bis(2-{2-methoxyethoxy}ethyl)-*9H*-fluoren-2-yl]benzo[*c*][1,2,5]thiadiazole-4-carbaldehyde (5)

Tetrakis(triphenylphosphine)palladium(0) (117 mg, 0.10 mg) followed by *t*-butanol (10 mL) were added to a mixture of 2-bromo-7-iodo-9,9-bis[2-(2-methoxyethoxy)ethyl]-*9H*-fluorene (see Supporting Information) (1.53 g, 2.7 mmol), 7-(4,4,5,5-tetramethyl-1,3,2-dioxaborolan-2-yl)benzo[*c*][1,2,5]thiadiazole-4-carbaldehyde[30] (837 mg, 2.9 mmol), aqueous potassium carbonate (2 M, 20 mL), and toluene (25 mL) that had been deoxygenated by placing under vacuum six times and following by backfilling with argon. The mixture was stirred at reflux under argon overnight in the dark. The mixture was allowed to cool to room temperature and diluted with diethyl ether (20 mL) and water (20 mL). The aqueous layer was isolated and extracted with diethyl ether (5 × 20 mL). The combined organic fractions were washed with water (2 × 20 mL), brine (2 × 50 mL), dried over anhydrous sodium sulfate, and filtered through a silica plug that was pre-washed with diethyl ether (~100 mL). The filtrate was collected, and the solvent was removed. The crude product was purified using flash column chromatography over silica with diethyl ether:toluene mixtures (0:1

to 1:1) as eluent to afford **5** as a bright orange oil (843 mg, 52%); found: C, 58.9; H, 5.1; N, 5.0; S, 5.1; $C_{30}H_{31}BrN_2O_5S$ requires: C, 58.9; H, 5.1; N, 4.6; S, 5.2; λ_{max}(CH_2Cl_2/nm): 240sh (log ε/dm^3 mol^{-1} cm^{-1} 4.05), 301 (4.52), 310 sh (4.49), 405 (4.36); IR (solid) ν/cm^{-1} = 1688 (C=O); δ_H (500 MHz, $CDCl_3$): 2.41−2.53 (4H, m, Gl−CH_2), 2.84−2.93 (4H, m, Gl−CH_2), 3.21−3.23 (4H, m, Gl−CH_2), 3.26 (6H, s, Gl−CH_3), 3.28−3.30 (4H, m, Gl−CH_2), 7.53 (1H, dd, *J* = 2.0, 8.0 Hz, Fl−H), 7.62 (1H, d, *J* = 1.0 Hz Fl−H), 7.63 (1H, d, *J* = 8.5 Hz, Fl−H), 7.84 (1H, dd, *J* = 1.0, 8.0 Hz, Fl−H), 7.97 (1H, d, *J* = 7.5 Hz, BT−H), 8.05-8.08 (2H, m, Fl−H), 8.34 (1H, d, *J* = 7.5 Hz, BT−H), 10.82 (1H, s, CHO); δ_C (125 MHz, $CDCl_3$): 39.5, 51.9, 59.0, 67.0, 70.0, 71.7, 120.1, 121.6, 122.1, 124.6, 126.3, 126.9(0), 126.9(4), 129.4, 130.8, 132.6, 135.8, 138.7, 140.3, 140.9, 149.3, 151.8, 153.8, 154.0, 189.0; *m/z* (ESI-HRMS) calcd. for $C_{30}H_{31}BrN_2O_5S$: 611.1210 (92%), 612.1241 (32%), 613.1194 (100%), 614.1222 (33%); found: 611.1233 (96%), 612.1275 (29%), 613.1211 (100%), 614.1245 (33%).

7,7'-[9,9,9',9'-Tetrakis(2-{2-methoxyethoxy}ethyl)-9*H*,9'*H*-(2,2'-bifluorene)-7,7'-diyl]bis[benzo[*c*][1,2,5]thiadiazole-4-carbaldehyde] (7)

[1,1'-Bis(diphenylphosphino)ferrocene]dichloropalladium(II) dichloromethane complex (66 mg, 0.08 mmol) was added to a mixture of **5** (926 mg, 1.5 mmol), bis(pinacol)diboron (472 mg, 1.8 mmol), anhydrous potassium acetate (491 mg, 5.0 mmol), and dry 1,4-dioxane (14.5 mL) that had been deoxygenated by placing under vacuum three times followed by backfilling with argon. The mixture was stirred at reflux under argon in the dark overnight. The mixture was allowed to cool to room temperature and filtered through a Celite® plug that was pre-washed with diethyl ether. The residue was washed thoroughly with dichloromethane (~150 mL). The filtrate was collected, and the solvent was removed. The crude product was purified using flash column chromatography over silica with *n*-hexane:diethyl ether:dichloromethane mixtures (1:1:0 then 1:2:1) as eluent to afford **6** as a bright orange solid (663 mg), which was used directly in the following reaction without further purification. Tetrakis(triphenylphosphine)palladium(0) (10 mg, 0.01 mmol) was added to a mixture of **5** (171 mg, 0.28 mmol), **6** (205 mg), aqueous potassium carbonate (2 M, 0.4 mL), toluene (1.6 mL) and *t*-butanol (0.2 mL) that had been deoxygenated under vacuum three times followed by backfilling with argon. The reaction mixture was stirred at reflux under argon in the dark for 40 h. The reaction was allowed to cool to room temperature before brine (20 mL) was added followed by dichloromethane (30 mL) and diethyl ether (60 mL). The aqueous layer was separated, and the organic fraction was washed with deionized water (3 × 30 mL). The organic fraction was then dried over anhydrous sodium sulfate, filtered, and the solvent was removed. The crude product was purified using MPLC over silica with a diethyl ether:methanol mixture (19:1) as eluent to afford an orange solid. The orange solid was dissolved in methanol (5 mL) and diethyl ether (45 mL) was added. The mixture was cooled in a dry ice/acetone bath and the precipitate was collected via vacuum filtration and dried under vacuum to afford **7** as a bright orange powder (170 mg, 59% based on the amount of **5** used in the second step); m.p.: 175−177 °C; λ_{max}(CH_2Cl_2/nm): 324 (log ε/dm^3 mol^{-1} cm^{-1} 5.11), 431 (5.01); IR (solid) ν/cm^{-1} = 1685 (C=O); δ_H (500 MHz, CD_2Cl_2): 2.51-2.60 (8H, m, Gl−CH_2), 2.92-3.00 (8H, m, Gl−CH_2), 3.17 (12H, s, Gl−CH_3), 3.20-3.23 (8H, m, Gl−CH_2), 3.24-3.26 (8H, m, Gl−CH_2),

7.79 (2H, dd, J = 1.5, 8.0 Hz, Fl−H), 7.85 (2H, brd, J = 1.0 Hz, Fl−H), 7.92 (2H, d, J = 8.0 Hz, Fl−H), 7.95 (2H, d, J = 8.0 Hz, Fl−H), 8.03 (2H, d, J = 7.5 Hz, BT−H), 8.12 (2H, dd, J = 1.5, 8.0 Hz, Fl−H), 8.19 (2H, brd, J = 1.0 Hz, Fl−H), 8.34 (2H, d, J = 7.5 Hz, BT−H), 10.82 (2H, s, CHO); δ_C (125 MHz, CD_2Cl_2): 39.7, 51.9, 58.6, 67.1, 69.9, 71.8, 120.2, 120.8, 121.9, 124.7,126.3, 126.9, 127.1, 129.3, 132.2, 135.6, 139.3, 140.4, 141.1, 141.7, 150.1, 150.8, 154.1(3), 154.1(5), 188.9; *m/z* (ESI-HRMS) calcd. for $C_{66}H_{62}N_4O_{10}S_2Na$ $[M + Na]^+$: 1085.3800 (100%), 1086.3833 (65%), 1087.3867 (21%); found: 1085.3767 (100%), 1086.3799 (68%), 1087.3810 (31%).

2,2'-[({9,9,9',9'-Tetrakis[2-(2-methoxyethoxy)ethyl]-9*H*,9'*H*-[2,2'-bifluorene]-7,7'-diyl}bis{benzo[*c*][1,2,5]thiadiazole-7,4-diyl})bis(methaneylylidene)]dimalononitrile (Fluorenyl-dimer)

A mixture of **7** (53 mg, 0.05 mmol) and malononitrile (35 mg, 0.53 mmol) in chlorobenzene (2 mL) was deoxygenated by placing under vacuum three times followed by backfilling with argon. The reaction mixture was then stirred in an oil bath held at 75 °C under argon. Pyridine (0.1 mL) was added to the reaction mixture, which was then stirred in an oil bath held at 75 °C under argon overnight. The solvent was removed and the crude product was purified using MPLC over silica with a diethyl ether:methanol mixture (19:1) as eluent to afford a dark red solid. The solid was dissolved in ethyl acetate (5 mL) and then *n*-hexane (30 mL) was added. The mixture was cooled in a dry ice/acetone bath and the precipitate that formed was collected at the filter, which was then washed with *n*-hexane (20 mL), and dried under vacuum to afford **Fluorenyl-dimer** as a bright red solid (20 mg, 37%); m.p.: 71 °C (DSC); $\lambda_{max}(CH_2Cl_2/nm)$: 336 (log ε/dm^3 mol^{-1} cm^{-1} 4.72), 481 (4.70); IR (solid) ν/cm^{-1} = 2226 (C≡N); δ_H (500 MHz, CD_2Cl_2): 2.51-2.60 (8H, m, Gl−CH_2), 2.91-3.00 (8H, m, Gl−CH_2), 3.17 (12H, s, Gl−CH_3), 3.20-3.22 (8H, m, Gl−CH_2), 3.24-3.26 (8H, m, Gl−CH_2), 7.79 (2H, dd, J = 1.5, 8.0 Hz, Fl−H), 7.85 (2H, d, J = 1.5 Hz, Fl−H), 7.92 (2H, d, J = 8.0 Hz, Fl−H), 7.96 (2H, d, J = 8.0 Hz, Fl−H), 8.06 (2H, d, J = 7.5 Hz, BT−H), 8.14 (2H, dd, J = 1.5, 8.0 Hz, Fl−H), 8.24 (2H, d, J = 1.5 Hz, Fl−H), 8.84 (2H, d, J = 7.5 Hz, BT−H), 8.91 (2H, s, VIN−H); δ_C (125 MHz, CD_2Cl_2): 39.7, 51.9, 58.6, 67.1, 69.9, 71.8, 83.3, 113.2, 114.0, 120.3, 120.9, 121.9, 122.6, 124.8, 126.9, 127.4, 129.4, 130.8, 135.2, 139.2, 140.5, 141.2, 142.1, 150.2, 150.9, 153.0, 153.2, 154.6; *m/z* (ESI-HRMS) calcd. for $C_{66}H_{63}N_8O_8S_2$ $[M + H]^+$: 1159.4205 (100%), 1160.4238 (71%), 1161.4272 (25%); found: 1159.4224 (100%), 1160.4252 (73%), 1161.4266 (38%); $T_{d(5\%)}$: 336 °C; DSC (heating rate: 50 °C min^{-1}/cooling rate: 100 °C): T_m = 71 °C (1st cycle − heating), T_g = 66 °C (2nd – 4th cycles – heating); $E_{1/2(red)}$ (CV/tetrahydrofuran): -1.2 V, -1.8 V.

7,7'-[9,9,9',9',9'',9''-Hexakis(2-{2-methoxyethoxy}ethyl)-9*H*,9'*H*,9''*H*-(2,2':7',2''-terfluorene)-7,7''-diyl]bis[benzo[*c*][1,2,5]thiadiazole-4-carbaldehyde] (9)

Tetrakis(triphenylphosphine)palladium(0) (15 mg, 0.01 mmol) was added to a mixture of **8**[41] (52 mg, 0.10 mmol), crude **6** (151 mg), caesium carbonate (99 mg, 0.30 mmol), and anhydrous toluene (1.5 mL) that had been deoxygenated by three freeze-pump-thaw cycles followed by backfilling with argon. The reaction mixture was stirred at reflux under argon in the dark for 22 h. The reaction was allowed to cool to room temperature before deionised water (10 mL) and dichloromethane (10 mL) were added sequentially. The

aqueous layer was separated and extracted with dichloromethane (3 × 10 mL). The combined organic fractions were dried over anhydrous sodium sulfate, filtered, and the solvent was removed. The crude product was purified using MPLC over silica using diethyl ether:methanol mixtures (100:0 then increasing to 93:7) as eluent to afford an orange solid. The solid was dissolved in diethyl ether (15 mL) and then the solution was cooled in a dry ice/acetone bath. The precipitate was collected via vacuum filtration and dried under vacuum to afford **9** as a bright orange powder (50 mg, 35%); m.p.: 68−69 °C; λ_{max}(CH_2Cl_2/nm): 330 (log ε/dm^3 mol^{-1} cm^{-1} 4.78), 349 (4.81), 425 (4.74); IR (solid) ν/cm^{-1} = 1689 (C=O); δ_H (300 MHz, $CDCl_3$): 2.58-2.66 (12H, m, Gl−CH_2), 2.90-3.01 (12H, m, Gl−CH_2), 3.24-3.35 (42H, m, Gl−CH_2 and −CH_3), 7.70-7.78 (8H, m, Fl−H), 7.84 (2H, d, J = 8.0 Hz, Fl−H), 7.88 (2H, d, J = 8.0 Hz, Fl−H), 7.92-7.95 (2H, m, Fl−H), 8.01 (2H, d, J = 7.5 Hz, BT−H), 8.10-8.13 (4H, m, Fl−H), 8.36 (2H, d, J = 7.5 Hz, BT−H), 10.83 (2H, s, CHO); *m/z* (ESI-HRMS) calcd. for $C_{83}H_{90}N_4O_{14}S_2$ [M]$^+$: 1430.5889 (100%), 1431.5923 (90%), 1432.5957 (40%), 1433.5990 (12%); found: 1430.5894 (37%), 1431.5957 (100%), 1432.5994 (80%), 1433.6012 (46%).

2,2'-[({9,9,9',9',9'',9''-Hexakis[2-(2-methoxyethoxy)ethyl]-9*H*,9'*H*,9''*H*-[2,2':7',2''-terfluorene]-7,7''-diyl}bis{benzo[*c*][1,2,5]thiadiazole-7,4-diyl})bis(methaneylylidene)]dimalononitrile (Fluorenyl-trimer)

A mixture of **9** (50 mg, 0.03 mmol) and malononitrile (35 mg, 0.53 mmol) in anhydrous chloroform (1.5 mL) was deoxygenated by placing under vacuum three times followed by backfilling with argon. Pyridine (0.1 mL) was added to the reaction mixture before it was stirred in an oil bath held at 75 °C under argon for 3.5 h. When the reaction mixture had cooled to room temperature, dichloromethane (30 mL) was added, and the mixture was washed with deionised water (30 mL). The aqueous fraction was then extracted with dichloromethane (3 × 10 mL). The combined organic fractions were dried over anhydrous sodium sulfate, filtered, and the solvent was removed under a stream of nitrogen. The crude product was purified by recrystallisation by dissolving in methanol followed by cooling the solution in a dry ice/acetone bath. The precipitate formed was collected at the filter, washed with cold methanol (10 mL), and dried under vacuum to afford **Fluorenyl-trimer** as a dark red powder (33 mg, 62%); λ_{max}(CH_2Cl_2/nm): 350 (log ε/dm^3 mol^{-1} cm^{-1} 4.93), 424sh (4.57), 471 (4.63); IR (solid) ν/cm^{-1} = 2226 (C≡N); δ_H (500 MHz, CD_2Cl_2): 2.53-2.59 (12H, m, Gl−CH_2), 2.89-3.01 (12H, m, Gl−CH_2), 3.18-3.27 (42H, m, Gl−CH_2 and −CH_3), 7.77 (2H, dd, J = 1.5, 8.0 Hz, Fl−H), 7.79 (2H, dd, J = 1.5, 8.0 Hz, Fl−H), 7.84 (4H, brdd, J = 1.0, 6.5 Hz, Fl−H), 7.87 (2H, d, J = 8.0 Hz, Fl−H), 7.92 (2H, d, J = 8.0 Hz, Fl−H), 7.94-7.96 (2H, m, Fl−H), 8.06 (2H, d, J = 7.5 Hz, BT−H), 8.14 (2H, dd, J = 1.5, 8.0 Hz, Fl−H), 8.24 (2H, brd, J = 1.0 Hz, Fl−H), 8.84 (2H, dd, J = 0.5, 7.5 Hz, BT−H), 8.91 (2H, s, VIN−H); δ_C (125 MHz, CD_2Cl_2): 40.0, 40.2, 52.0, 52.2, 58.9, 67.4, 70.2, 72.1, 72.2, 83.6, 113.5, 120.6, 120.7, 121.2, 122.1, 122.2, 122.9, 125.1, 127.1, 127.2, 127.7, 129.7, 131.1, 135.4, 139.3, 140.0, 140.7, 140.8, 141.7, 142.5, 150.6, 150.7, 151.2, 153.3, 153.5, 154.9; *m/z* (ESI-HRMS) calcd. for $C_{89}H_{90}N_8O_{12}S_2Na$ [M + Na]$^+$: 1549.6012 (100%), 1550.6045 (96%), 1551.6079 (46%), 1552.6112 (14%); found: 1549.5993 (100%), 1550.6027 (99%), 1551.6053 (62%), 1552.6078 (31%); $T_{d(5\%)}$: 345 °C; DSC (heating/cooling rate: 100 °C min^{-1}): T_g = 77 °C (heating – third cycle), 191 °C (reversible endothermic transition – first and subsequent cycles); $E_{1/2(red)}$ (CV/tetrahydrofuran): -1.2 V, -1.8 V.

Conflicts of interest

There are no conflicts to declare.

Acknowledgement

The work was carried at the Centre for Organic Photonics & Electronics at The University of Queensland. WJ acknowledges the Australian Centre for Advanced Photovoltaics Fellowship. This program has been supported by the Australian Government through the Australian Renewable Energy Agency (ARENA). The Australian Government, through ARENA, is supporting Australian research and development in solar photovoltaic and solar thermal technologies to help solar power become cost competitive with other energy sources. The views expressed herein are not necessarily the views of the Australian Government, and the Australian Government does not accept responsibility for any information or advice contained herein. PLB is an Australian Research Council Laureate Fellow (FL160100067). The authors acknowledge Drs Dani Stoltzfus and Kinitra Hutchinson for the preparation of **CPDT-dimer**. This work used computational resources provided by the Australian Government through the National Computational Infrastructure under the National Computational Merit Allocation Scheme. This work was performed in part at the Queensland node of the Australian National Fabrication Facility (ANFF-Q): a company established under the National Collaborative Research Infrastructure Strategy to provide nano and micro fabrication facilities for Australia's researchers. This work was also performed in part at the SAXS/WAXS beamline at the Australian Synchrotron, part of ANSTO.

References

[1] Y. Cui, H. Yao, J. Zhang, K. Xian, T. Zhang, L. Hong, Y. Wang, Y. Xu, K. Ma, C. An, C. He, Z. Wei, F. Gao, J. Hou, *Adv. Mater.* **2020**, *32*, 1908205.

[2] L. Hong, H. Yao, Z. Wu, Y. Cui, T. Zhang, Y. Xu, R. Yu, Q. Liao, B. Gao, K. Xian, H. Y. Woo, Z. Ge, J. Hou, *Adv. Mater.* **2019**, *31*, 1903441.

[3] B. Kan, J. Zhang, F. Liu, X. Wan, C. Li, X. Ke, Y. Wang, H. Feng, Y. Zhang, G. Long, R. H. Friend, A. A. Bakulin, Y. Chen, *Adv. Mater.* **2018**, *30*, 1704904.

[4] C. Zhu, J. Yuan, F. Cai, L. Meng, H. Zhang, H. Chen, J. Li, B. Qiu, H. Peng, S. Chen, Y. Hu, C. Yang, F. Gao, Y. Zou, Y. Li, *Energy & Environ. Sci.* **2020**, *13*, 2459.

[5] L. Zuo, X. Shi, S. B. Jo, Y. Liu, F. Lin, A. K.-Y. Jen, *Adv. Mater.* **2018**, *30*, 1706816.

[6] L. Zhu, M. Zhang, G. Zhou, T. Hao, J. Xu, J. Wang, C. Qiu, N. Prine, J. Ali, W. Feng, X. Gu, Z. Ma, Z. Tang, H. Zhu, L. Ying, Y. Zhang, F. Liu, *Adv. Energy Mater.* **2020**, *10*, 1904234.

[7] X. Song, N. Gasparini, L. Ye, H. Yao, J. Hou, H. Ade, D. Baran, *ACS Energy Lett.* **2018**, 3, 669.

[8] R. Xue, J. Zhang, Y. Li, Y. Li, *Small* **2018**, *14*, 1801793.

[9] F. Di Maria, M. Biasiucci, F. P. Di Nicola, E. Fabiano, A. Zanelli, M. Gazzano, E. Salatelli, M. Lanzi, F. Della Sala, G. Gigli, G. Barbarella, *J. Phys. Chem. C* **2015**, *119*, 49, 27200.

[10] J. H. Lee, C. G. Park, A. Kim, H. J. Kim, Y. Kim, S. Park, M. J. Cho, D. H. Choi, *ACS Appl. Mater. Interfaces* **2018**, *10*, 18974.

[11] Y. He, N. Li, C. J. Brabec, *Org. Mater.* **2021**; *3*, 228.

[12] S. Lucas, J. Kammerer, M. Pfannmöller, R. R. Schröder, Y. He, N. Li, C. J. Brabec, T. Leydecker, P. Samorì, T. Marszalek, W. Pisula, E. Mena-Osteritz, P. Bäuerle, *Sol. RRL* **2021**, *5*, 2000653.

[13] W. Wang, R. Sun, J. Guo, J. Guo, J. Min, *Angew. Chem. Int. Ed.* **2019**, *58*, 14556.

[14] Y. He, T. Heumüller, W. Lai, G. Feng, A. Classen, X. Du, C. Liu, W. Li, N. Li, C. J. Brabec, *Adv. Energy Mater.* **2019**, *9*, 1900409.

[15] G. Feng, J. Li, Y. He, W. Zheng, J. Wang, C. Li, Z. Tang, A. Osvet, N. Li, C. J. Brabec, Y. Yi, H. Yan, W. Li, *Joule* **2019**, *3*, 1765.

[16] L. J. A. Koster, S. E. Shaheen, J. C. Hummelen, *Adv. Energy Mater.* **2012**, *2*, 1246.

[17] J. Brebels, J. V. Manca, L. Lutsen, D. Vanderzande, W. Maes, *J. Mater. Chem. A* **2017**, *5*, 24037.

[18] B. A. Gregg, M. C. Hanna, *J. Appl. Phys.* **2003**, *93*, 3605.

[19] Q. Lin, A. Armin, R. C. R. Nagiri, P. L. Burn, P. Meredith, *Nat. Photon.* **2015**, *9*, 106.

[20] S. Collavini, S. F. Völker, J. L. Delgado, *Angew. Chem. Int. Ed.* **2015**, *54*, 9757.

[21] J. E. Donaghey, A. Armin, D. M. Stoltzfus, P. L. Burn, P. Meredith, *Chem. Comm.* **2016**, *52*, 13714.

[22] M. P. Hughes, K. D. Rosenthal, N. A. Ran, M. Seifrid, G. C. Bazan, T.-Q. Nguyen, *Adv. Funct. Mater.* **2018**, *28*, 1801542.

[23] X. Chen, Z. Zhang, Z. Ding, J. Liu, L. Wang, *Angew. Chem. Int. Ed.* **2016**, *55*, 10376.

[24] S. Torabi, F. Jahani, I. Van Severen, C. Kanimozhi, S. Patil, R. W. A. Havenith, R. C. Chiechi, L. Lutsen, D. J. M. Vanderzande, T. J. Cleij, J. C. Hummelen, L. J. A. Koster, *Adv. Funct. Mater.* **2015**, *25*, 150.

[25] A. Armin, D. M. Stoltzfus, J. E. Donaghey, A. J. Clulow, R. C. R. Nagiri, P. L. Burn, I. R. Gentle, P. Meredith, *J. Mater. Chem. C* **2017**, *5*, 3736.

[27] S. Sami, R. Alessandri, R. Broer, R. W. A. Havenith, *ACS Appl. Mater. Interfaces* **2020**, *12*, 17783.

[28] S. Kraner, C. Koerner, K. Leo, E. Bittrich, K. J. Eichhorn, Y. Karpov, A. Kiriy, M. Stamm, K. Hinrichs, M. Al-Hussein, *Phys. Rev. B* **2015**, *91*, 195202.

[29] B. Meng, H. Song, X. Chen, Z. Xie, J. Liu, L. Wang, *Macromolecules* **2015**, *48*, 4357.

[30] A. Wadsworth, C. Nielsen, S. Holliday, I. McCulloch, M. Kirkus, D. Baran, S. Ashraf, International Patent WO2017/191644 A1, May 6, **2016**.

[31] G te Velde, F. M. Bickelhaupt, E. J. Berends, C. F. Guerra, S. J. A. van Gisbergen, J. G. Sniders, T Ziegler, *Comput. Chem.* **2001**, *22*, 931.

[32] J. Nath, S. K. Mishra, *Fluid Phase Equil.* **1998**, *145*, 89.

[33] M. Stolterfoht, A. Armin, S. Shoaee, I. Kassel, P. Burn, P. Meredith, *Nat. Commun.* **2016**, *7*, 11944.

[34] C. W. Tang, *Appl. Phys. Lett.* **1986**, *48*, 183.

[35] J. Li, F. Dierschke, J. Wu, A. C. Grimsdale, K. Müllen, *J. Mater. Chem.* **2006**, *16*, 96.

[36] R. Y. C. Shin, T. Kietzke, S. Sudhakar, A. Dodabalapur, Z.-K. Chen, A. Sellinger, *Chem. Mater.* **2007**, *19*, 1892.

[37] M. Stolterfoht, A. Armin, B. Philippa, R. D. White, P. L. Burn, P. Meredith, G. Juška, A. Pivrikas, *Sci. Rep*. **2015**, 5, 9949.

[38] L. J. A. Koster, M. Kemerink, M. M. Wienk, K. Maturová, R. A. J. Janssen, *Adv. Mater.* **2011**, *23*, 1670.

[39] N. M. Kirby, S. T. Mudie, A. M. Hawley, D. J. Cookson, H. D. T. Mertens, N. Cowieson, V. Samardzic-Boban, *J. Appl. Cryst.* **2013**, *46*, 1670.

[40] J. Ilavsky, *J. Appl. Cryst.* **2012**, *45*, 324.

[41] S. Gug, F. Bolze, A. Specht, S. Bourgogne, M. Goeldner, J-F. Nicoud, *Angew. Chem. Int. Ed*. **2008**, *47*, 9525.